Journal of Hazardous Materials 488 (2025) 137450

Contents lists available at ScienceDirect

Journal of Hazardous Materials

journal homepage: www.elsevier.com/locate/jhazmat

Amphipathic regulation of cottonseed protein with the conjugation of bayberry tannin for efficient surface decontamination of uranium

Kwame Eduam Baiden Frempong [a,1], Jie Wang [b,1], Yu Chen [a], Xiaobo Liu [d], Akosua Nyame Adom Frempong [e], Xiaofang Liang [b], Meng Kuang [c], Yanxia Wei [a,*], Min Xue [b,*], Jian Zhou [a,*]

[a] School of Life Science and Engineering, School of Materials and Chemistry, Engineering Research Center of Biomass Materials, Ministry of Education, Southwest University of Science and Technology, Mianyang, Sichuan 621010, PR China
[b] Institute of Feed Research, Chinese Academy of Agricultural Sciences, Beijing 100081, PR China
[c] Institute of Cotton Research of Chinese Academy of Agricultural Sciences/National Key Laboratory of Cotton Bio-breeding and Integrated Utilization, Anyang, Henan 455000, PR China
[d] Xinjiang Herun Jinlan Biological Technology Co., Ltd., Yili, Xinjiang 833299, PR China
[e] Department of Nutrition and Food Science, University of Ghana, Legon, Accra, Ghana

HIGHLIGHTS

- Novel eco-surfactant were synthesised from cottonseed and bayberry tannin via Free-Radical grafting.
- CPI-BT showed good UO_2^{2+} removal capacity in aqueous environment.
- CPI-BT showed effective decontamination of UO_2^{2+}-contaminated fabric and other solid surfaces.
- Removal mechanism involved chelation by the phenolic hydroxyl, amino, and carboxyl groups.

GRAPHICAL ABSTRACT

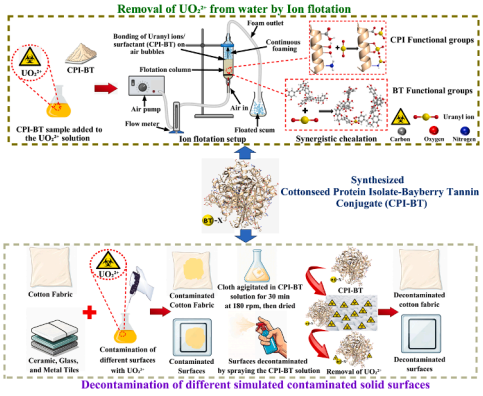

ARTICLE INFO

Editor:

Keywords:
Cottonseed protein
Bayberry tannin
Conjugate
Surfactant
Uranyl ion

ABSTRACT

Radioactive substances (Uranium) on the human body or facility surfaces are easy to diffuse in nuclear activity, posing a severe threat to ecological security and human health, especially for personnel working in and around uranium mining and nuclear facilities. In this work, a green protein-based surfactant was synthesized using the free-radical conjugating method to graft bayberry tannin (BT) onto cottonseed protein (CPI) for regulating its amphipathy and removing uranyl ions (UO_2^{2+}) in both aqueous environments and solid surfaces. FTIR, CD spectroscopy, intrinsic fluorescence, conductometric titration, and SEM-EDX characterization techniques confirmed the successful covalent conjugation of BT onto CPI, inducing unfolding, conformational changes, and

* Corresponding authors.
E-mail addresses: weiyx@swust.edu.cn (Y. Wei), xuemin@caas.cn (M. Xue), zhoujian@swust.edu.cn (J. Zhou).
[1] These authors contributed equally to this work and should be considered co-first authors.

https://doi.org/10.1016/j.jhazmat.2025.137450
Received 6 December 2024; Received in revised form 28 January 2025; Accepted 29 January 2025
Available online 30 January 2025

enhanced hydrophilicity of CPI. Thus, leading to improved foaming and emulsifying properties. Notably, the surfactant exhibited high efficiency in UO_2^{2+} removal and selectivity from an aqueous environment, achieving a removal rate of 93 % within 30 minutes and a maximum adsorption capacity of 310.15 mg/g. Additionally, it also demonstrated effectiveness in decontaminating different simulated uranium-contaminated solid surfaces. The synergistic interaction between BT's phenolic-hydroxyl groups and CPI's structural versatility and functional groups facilitated the effective UO_2^{2+} complexation. This study demonstrates the feasibility of using agro-industrial waste-derived CPI-BT as an eco-friendly, sustainable, and cost-effective alternative to synthetic surfactants for mitigating uranium contamination in environments near uranium mining operations and nuclear facilities.

1. Introduction

Nuclear energy is regarded as a critical candidate for meeting future energy demands due to its efficiency and cleanliness, with uranium currently the most essential nuclear fuel, and its stable supply implies nuclear energy's long-term development [1,2]. However, as a result of improper disposal of nuclide-containing wastewater from large-scale nuclear power, unpredictable nuclear accidents, nuclear waste post-treatment, leakage, terrestrial uranium ore mining, military action, and other accidents, radioactive uranium has been discharged into the environment, posing a severe threat to human health and ecological security [1,3]. A significant occupational health and safety risk arises from the ubiquitous exposure of the workforce to radioactively contaminated surfaces during the daily operation and decommissioning of nuclear facilities [4]. Direct contact with uranium contaminants can result in their adsorption onto the skin, facilitating entry into the bloodstream and accumulation in vital organs, posing both chemical and radiological toxicity [5]. Delayed decontamination may result in the penetration of radionuclides deep into the surfaces or the generation of aerosols in the air, potentially causing radioactive contamination that is challenging to eradicate [4,6]. For these reasons, effective and timely surface-level radioactive decontamination research is as vital as environmental remediation.

Currently, chemical precipitation, oxidization, and adsorption are the conventional techniques to remove metal ions from aqueous environments [7,8]. However, these techniques are often limited by high operational costs, low performance, and potential secondary pollution [9]. In contrast, ion flotation offers significant advantages, such as shorter processing time, simple operation, removal of trace metal ions from large volumes of wastewater, reduced waste production, low energy consumption, and ion selectivity [10,11]. Synthetic surfactants, such as cetyltrimethylammonium bromide, dodecyl diethylenetriamine, and many more, have been widely utilized in ion flotation processes due to their efficacy in facilitating separation. However, they exhibit several drawbacks, including significant environmental impacts, unstable chemical characteristics, bioaccumulation, high cost, and limited biodegradability [12,13]. Furthermore, effective metal ion recovery from the foamate presents a significant challenge. Hence, there is a higher demand for environmentally safer options in the industrial application of ion flotation.

Surfactants are surface active amphiphiles that serve multiple purposes, are found in various consumer and industrial products, and are essential to numerous industrial operations. Most surfactants currently in use are synthetic; however, their application directly or indirectly may be hazardous to health and the environment [14]. The global surfactant production was about 14.1 million tons in 2017 [15], with about 60 % of the total output re-deposited into the environment [16]. In today's environmentally conscious world, surfactants should be less toxic, biodegradable, and surface-active. The potential of natural surfactants as replacements with similar functionality and properties while mitigating the environmental consequences is of high interest. Biosurfactants such as microbial surfactants represent the next generation of industrial surfactants, as they fulfill most criteria for low environmental impact and can be tailor-synthesized [15]. However, low productivity, high downstream production costs, and insufficient knowledge regarding their production in bioreactor systems limit their application [17]. Despite their properties, the high cost of synthesizing several biosurfactants restricts their widespread application in large-scale wastewater treatment processes [11,12]. Developing sustainable, functional, and cost-effective surfactants is warranted to overcome these environmental, technical, and economic defects.

A promising natural plant fiber source, cotton (*Gossypium hirsutum* L.), is grown in over 80 countries worldwide [18]. After stripping cotton from the seed and oil extraction, cottonseed meal is the primary waste product obtained, which is rich in high-quality protein with excellent composition and has been touted as a tremendous potential plant protein source [19,20]. Cottonseed protein isolates (CPI) display a wide range of bioactivities, good emulsifying and foaming properties, fluorescence intensity, and oil/water absorption capacity, which points to their potential use in multiple industries [18,21]. The use of CPI in non-food applications, including adhesives, bioplastics, and interfacial applications, has also garnered much attention recently [19]. Nevertheless, its application in certain fields is limited because CPI predominantly comprises folded globular proteins characterized by large molecular weight, which diminishes their reactive activity and results in inadequate amphiphilicity [18,20,22]. Researchers are interested in phenolic compounds because of their wide availability, and they have been shown to provide structural and beneficial functionalities [23]. Tannin is a low-cost, renewable natural compound with multiple binding sites that enable various interactions with alkaloids, polysaccharides, proteins, metal ions, and other chemicals [24]. This makes it useful for metal adsorption, antioxidants, leather tanning agents, and many more [25]. Tannin molecules have a significant complexation capacity with UO_2^{2+} [2]. However, its high solubility makes it challenging to use in an aqueous environment and needs to be modified to be effective. In previous studies, immobilizing tannin onto proteins such as bovine serum albumin and collagen improved the adsorption capacity of metal ions [2,26,27]. The interaction of tannin with protein weakens the hydrophobicity, and its polyphenolic groups enhance surface hydrophilicity, leading to an improved amphiphilicity [28]. They can also chelate metal ions, attributed to multiple phenolic hydroxyl groups in the molecules [29]. Plant proteins and polyphenols can interact in various complex ways, including covalent and/or noncovalent interactions, creating new bioactive substances with multi-functional properties [23,30,31]. Currently, polyphenol-protein conjugates are synthesized through any of these conjugation reaction methods: physical, alkaline, free-radical, and enzyme-catalyzed grafting [32]. The free radical method is preferred over the others because it is fast and safe, room-temperature initiated grafting, offers permanent conjugation (covalent), potentially leading to more durable functional modification, and prevents polyphenol degradation compared to conventional alkaline and enzymatic procedures [33].

Both CPI and BT are natural materials considered biodegradable with astringent activities and possess various structural and functional properties. In this study, we present the modification reaction that involves the covalent conjugation of BT onto CPI using the green chemistry free radical-mediated conjugation method. This improved the amphiphilicity, structural and functional properties, and adsorption

behavior in both aqueous environments and solid surfaces. The ability to graft polyphenols onto proteins is an intriguing development that greatly enhances the functionality of biomacromolecules and opens up new possibilities for their application and a strategic approach for removing UO_2^{2+} from both aqueous environment and solid surfaces.

2. Materials and method

2.1. Materials

Cottonseed meal (CSM) (protein content at 60–65 %) was obtained from Xinjiang Jinlan Plant Protein Co. Ltd. (China). Bayberry tannin was obtained from Baise Forest Chemical General Plant. All reagents used were of analytical grade, and a standard solution of uranium was purchased from the Beijing Institute of Chemical Metallurgy for Nuclear Industry.

2.2. Synthesis of cottonseed protein isolate – bayberry tannin conjugate (CPI-BT)

The KOH extraction method described in our previous studies was used to obtain cottonseed protein isolate (CPI) [34]. The ascorbic acid/H_2O_2 redox pair initiator system was used to prepare the CPI-BT conjugate as described previously with slight modifications [35]. Exactly 20 g of CPI was dispersed in 500 mL of distilled water under a slow stream of N_2 gas. Next, 5 mL of redox initiator compound (H_2O_2 (1.0 M) comprising 0.5 g of ascorbic acid) was added to the CPI dispersion. After 2 h, different concentrations (0.35, 0.70, and 1.05 mM) of BT were added and stirred at room temperature. After 24 h of reaction, the unreacted BT was removed by dialysis until no free polyphenol existed in the system. The solution was freeze-dried, and the conjugated CPI-BT 0.35 mM, CPI-BT 0.70 mM, and CPI-BT 1.05 mM powder was obtained.

2.3. Determination of polyphenol binding ratio and binding efficiency

As previously described, the CPI and BT conjugation efficiency was determined by dialyzing the complex against 20 % DMSO at 4 ℃ for 24 h, with minor modifications [30,36]. The Folin-ciocalteu (FC) technique measured the dialyzed polyphenol concentration. In a 10 mL centrifuge tube, 1 mL of sample solution, 3 mL of ultra-pure water, 1 mL of 1 M FC reagent, and 3 mL 7.5 % Na_2CO_3 were mixed thoroughly. The absorbance of the mixture was measured at 765 nm using a UV–visible spectrophotometer (UV-5500 PC, Metash, China) after 1 h of incubation in the dark. Gallic acid (0–0.25 mg/mL) was used as standard, and the binding ratio and substitution degree were calculated as follows:

$$Binding\ ratio(\%) = \frac{Total\ BT - BT\ dialyzed}{Total\ BT} \times 100 \quad (1)$$

$$Subsitution\ degree\ of\ polyphenol(\mu M \Big/ g_{CPI}) = \frac{Substitution\ of\ BT\ on\ CPI(\mu M)}{gof\ CPI} \quad (2)$$

2.4. CPI-BT characterization

2.4.1. Structural characterization

Fourier transform infrared spectroscopy (FTIR) spectra of CPI-BTs were carried out using Nicolet-6700 (Perkin Elmer Instruments Corporation). Circular dichroism (CD) spectroscopy measurement of the CPI-BT samples was carried out with a MOS-450 spectrometer, and the spectra were obtained from 190 to 260 nm. The binding energy of the elements of CPI-BT was measured by XPS ESCALAB250 (Thermo Fisher Corporation, USA). SEM-EDX analysis of the samples was observed by scanning electron microscope (Sigma 300, Zeiss, Germany) equipped with Energy dispersive X-ray spectroscopy (EDX) (Oxford Instrument X-Max, UK).

2.4.2. Physicochemical properties analysis

The carboxyl contents, represented as the mole number of the carboxyl group per gram of the protein ($Mol_{COOH}/g_{peptide}$), were determined by conductometric titration as described in a previous study [34].

The ζ-potential analysis of CPI-BT was evaluated using a Zeta potential analyzer (ZetaPALS, Brookhaven Instruments Corporation, USA). The surface tension of different concentrations of CPI-BT dispersions was analyzed using a tensiometer K100 (Kruss Scientific Instruments Ltd., Germany) with the Du Noüy ring method.

The contact angle of the CPI-BT solution was measured with a tensiometer K100 (Kruss, Germany) using the sessile drop approach in natural light.

The intrinsic fluorescence of CPI-BT (1 mg/mL) in phosphate buffer (100 mM, pH 7.0) was evaluated using a microplate reader (Thermo Varioskan Flash Multi Detection Reader, USA). The excitation wavelength was 280 nm, and the emission range was from 300 to 500 nm; the constant slit of 5 nm was set for both excitation and emission. The Stern-Volmer equation was used to analyze the fluorescence data to examine the interaction between CPI and BT.

$$\frac{F_0}{F} = 1 + k_q \tau_0 [Q] = 1 + K_{SV}[Q] \quad (3)$$

where F_0 and F are the intrinsic fluorescence of CPI before and after conjugation with BT, respectively, K_q is the quenching constant of the biological molecule; τ_0 is the average lifetime of fluorescent molecules without BT ($\tau_0 = 10^{-8}$ s); [Q] is BT concentration, K_{SV} is the fluorescence quenching constant.

The F_0/F against [Q] curve generally exhibits a linear curve. It may, however, exhibit an upward curve that concaves towards the y-axis in certain instances, suggesting the development of an apparent static quenching or sphere of action [30]. In this case, the apparent static form of the Stern-Volmer equation was applied as follows:

$$\frac{F_0}{F} = (1 + K(Q))\exp\left(\frac{[Q]VN}{1000}\right) \quad (4)$$

where N is the Avogadro's constant, and V is the sphere's volume. Eq. 4 could become Eq. 5 when K(Q) is low enough [37].

$$\frac{F_0}{F} = e^{(K_{FQ}[Q])} \quad (5)$$

where K_{FQ} is the fluorescence quenching constant for the apparent static model.

2.4.3. Functional properties analysis

The foaming capacity and stability (FC and FS) of CPI-BT were evaluated as described in a previous report with some modifications [21]. Exactly 25 mL (V_i) of the sample solution (1 mg/mL) was homogenized at 10,000 rpm for 1 min using a homogenizer (XHF-D H-SPEED, China). The whipped dispersion was quickly transferred into a measuring cylinder, and the volume of the foam was measured immediately (V_o) and then after 30 min (V_t).

The emulsifying activity and stability indexes (EAI and ESI) of CPI-BT were evaluated as described previously with some modifications [38]. Exactly 3 mL of medium-chain triglyceride oil (MCT) was added to a 9 mL sample solution and homogenized for 1 min at 10,000 rpm. Then, 50 μL of the emulsion was removed at 0 and 10 min from the bottom of the tube, immediately diluted with 5 mL of 0.1 % SDS solution, and mixed. Afterward, the absorbance was measured at 500 nm.

2.5. Ion flotation

CPI-BT's ability to remove UO_2^{2+} and the effects of pH, sample

dosage, ventilatory capacity, equilibrium time, presence of coexisting ions, and initial concentration on the removal capacity was investigated using the ion flotation method as described in a previous study [25]. The test was conducted at room temperature in the foaming apparatus, which consisted of a 30 cm long column with a 3 cm diameter and a porous sinter that can form tiny bubbles with a diameter of ~0.2 cm. The UO_2^{2+} concentration after the test was measured with a spectrophotometer. To make the UO_2^{2+} solution, a specific amount of uranyl nitrate was weighed, and then it was adjusted to the necessary pH using 0.1 M NaOH/HNO_3 to yield a particular pH solution. Approximately 100 mL UO_2^{2+} solution was placed into a conical flask and thoroughly mixed with a specific amount of CPI-BT. It was then transferred to the ion flotation apparatus, which is connected to an air pump to create foam in the column. The samples were taken at a height of about 5 cm above the sinter. The foam was also collected in a conical flask using an outlet tube. Arsenazo III was used as the complexing and color-developing agent for detecting UO_2^{2+} after the test. The removal quantity and removal rate (RE) of UO_2^{2+} unto CPI-BT were expressed as follows:

$$Q_e = \frac{(C_0 - C_e)V}{W} \tag{6}$$

$$RE(\%) = \frac{(C_0 - C_e)}{C_0} \times 100 \tag{7}$$

where C_0 and C_e are the concentration of UO_2^{2+} (mg/L) before and after removal, V is the volume of solution (L), Q_e is the removal amount of UO_2^{2+} (mg/g); W is the mass of CPI-BT (g).

The data of equilibrium time of UO_2^{2+} removal was fitted using the pseudo-first-order and pseudo-second-order. The nonlinear expression of the pseudo-first-order and pseudo-second-order are respectively as follows:

$$q_t = q_e(1 - \exp^{(-K_1 t)}) \tag{8}$$

$$q_t = \frac{K_2 \times t \times q_e^2}{(1 + (K_2 \times t \times q_e))} \tag{9}$$

where t is the reaction time (min), q_e and q_t represent the removal amount at any time and equilibrium, respectively (mg/g), K_1 is the rate constant of pseudo-first-order adsorption (g mg^{-1} min^{-1}), and K_2 is the rate constant of pseudo-second-order adsorption (g mg^{-1} min^{-1}).

The Langmuir and Freundlich models fitted the data of initial concentration on UO_2^{2+} removal, and the expressions are as follows respectively:

$$q_e = \frac{q_{max} \times K_L \times C_e}{(1 + (K_L \times C_e))} \tag{10}$$

$$q_e = K_F \times C_e^{\frac{1}{n}} \tag{11}$$

where q_e represents the equilibrium removal amount of UO_2^{2+} on the adsorbent (mg/g), q_{max} represents the saturated removal capacity in the Langmuir model (mg/g), K_L is a constant of the Langmuir model which is determined by the exchange equilibrium constant (L/mg), K_F is the Freundlich constant (mg/g)$(L/mg)^{1/n}$, and 1/n is a coefficient that indicates the non-uniformity of the adsorption site.

2.6. Decontamination of simulated uranium contamination on fabric material and other surfaces

A cotton fabric was used with an area of 5 cm × 5 cm. Before contamination, its natural background value A_0 was measured using a surface contamination meter (RJ39–2060, Shanghai Ergonomics Detecting Instrument Co. Ltd., China). It was contaminated by soaking it with 1 mL 4.75 g/L uranium solution and then drying it in an oven. The radioactivity value A_1 was measured after the contamination. The dried fabric was decontaminated by agitating it with water/CPI-BT solution for 30 min at 180 rpm. Afterward, the fabric was dried, and its radioactivity value A_2 was measured. Experimental plates of different materials with an area of 10 cm × 10 cm were washed and dried until the surface was parched. An area of 5 cm × 5 cm was demarcated in the center of each plate for contamination and testing similar to the above procedure. The difference was the decontamination step; the prepared CPI-BT solution was sprayed on the contaminated surface and allowed to sit for 30 min, or a swab soaked in the CPI-BT solution was used to wipe the plate instead. The decontamination rate (DR) was calculated as follows:

$$DR(\%) = \frac{(A_1 - A_0) - (A_2 - A_0)}{A_1 - A_0} \times 100 \tag{12}$$

2.7. Statistical analysis

The results were analyzed using Excel 2021 (Microsoft) and Origin Pro 2022 (Origin Lab Corporation, USA). Data were expressed as the mean ± standard error and were subjected to one-way ANOVA analysis (Tukey's HSD test) was carried out to find significant differences ($P < 0.05$) among conjugate and control samples.

3. Results and discussion

3.1. Synthesis of CPI-BT conjugates

The free-radical mediated grafting method was used to synthesize the CPI-BT conjugates. Achieving free-radical grafting at room temperature is feasible, which reduces the degradation of proteins or polyphenols [39]. This process uses the ascorbic acid/hydrogen peroxide redox pair as a starting system, making it suitable for application in food, pharmaceutical, and nonfood industries due to its cost-effectiveness, safety, and environmental friendliness [29]. Polyphenols form covalent bonds with proteins, primarily interacting with free amino groups (lysine), sulfhydryl groups (SH, cysteine), and other residues (such as histidine, methionine, proline, tryptophan, and tyrosine) [40]. A potential mechanism for BT binding to the side chains of CPI was proposed, as shown in Fig. 1A and B. Hydrogen peroxide can oxidize ascorbic acid to form ascorbate and hydroxyl radicals; this hydroxyl radicals can then attack H-atoms on the side chains of protein molecules to form protein macro-radicals, which can then react with the polyphenols' phenolic ring to form a covalent bond [35,41]. It is well known that polyphenols are excellent hydrogen donors and can form bonds with the O, NH, and S groups of proteins [35,42]. Molecular docking visualizes protein-polyphenol interaction and predicts the binding locations and forces between proteins and polyphenols [30]. Fig. 1C depicts the lowest binding energy between BT and CPI's amino acid residues. Hydrogen bond and hydrophobic interaction are the dominant binding forces between CPI and BT. Molecular docking mainly anticipates non-covalent interactions rather than covalent bonds, with limited research identifying binding sites and amino acid residues contributing to polyphenol-protein covalent complexes [40]. In this study, CPI-BT complexes formed a hydrogen bond with Val 148 (2.221 Å), two hydrogen bonds with Tyr 62 (2.110 Å and 2.397 Å), and a hydrophobic interaction with Lys 64 (2.166 Å).

Since conjugation significantly influences the bioactivity characteristics and other performance, the polyphenol content is a crucial factor in determining the functionality of CPI-BT conjugates. The amount of polyphenol bound to the protein is shown in Fig. S1A. The binding equivalent significantly increased with increment in BT concentration (0.35 – 1.05 mM). At 1.05 mM of BT, a maximum of 108.88 BTE mg/g was observed. This could be due to the increased chances for nucleophilic addition at high BT concentrations, which increases the degree of cross-linking. A similar trend was observed in the conjugation of gallic

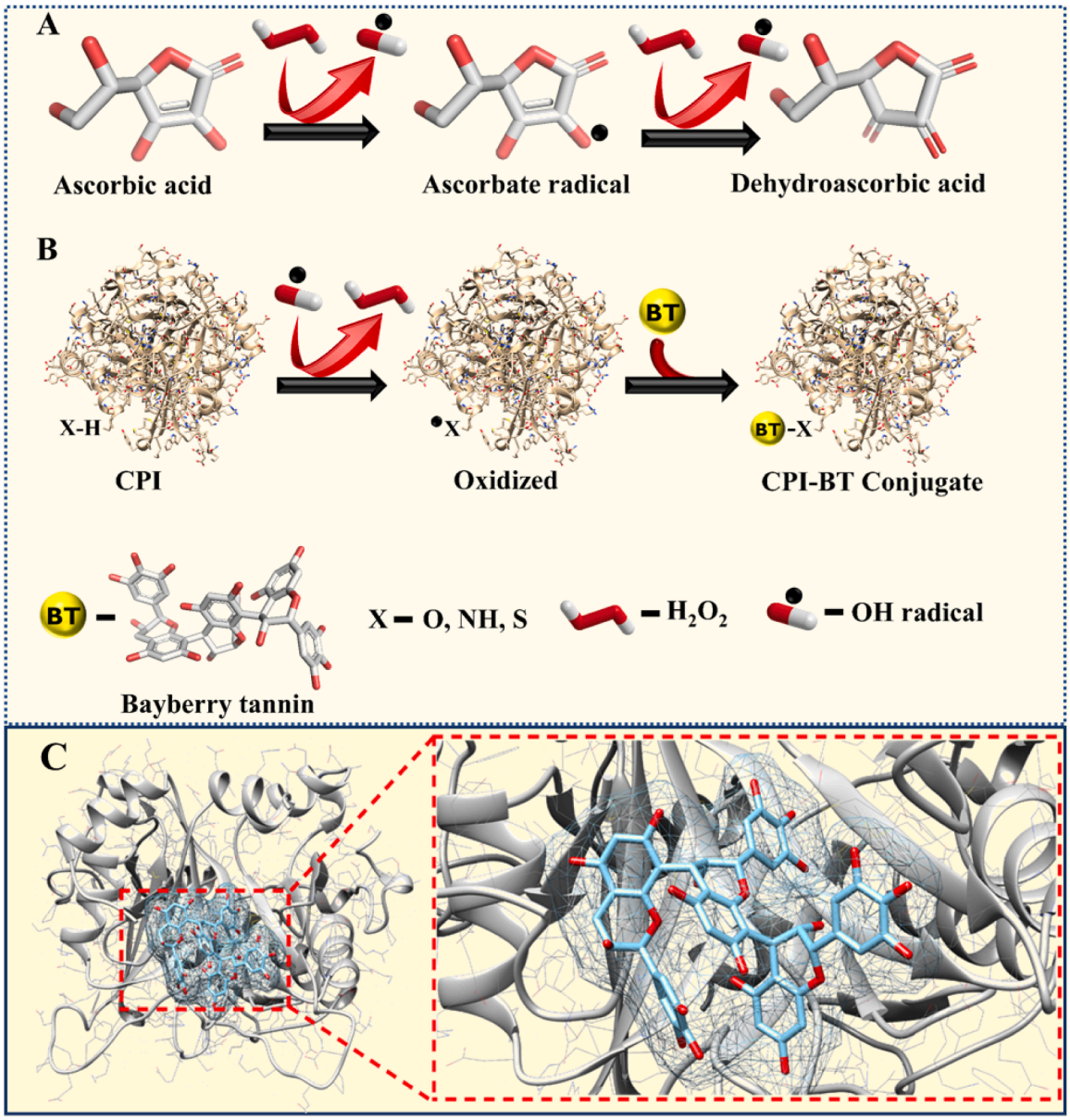

Fig. 1. Schematic representation of the mechanism of the covalent conjugation reaction of BT and CPI: Ascorbic acid oxidation system (A), CPI-BT radical conjugation reaction (B), and the 3D molecular docking mode between CPI and BT.

acid with myofibrillar protein [23] and rosemary, thyme, and basil polyphenols with soy protein isolate [39]. The binding efficiency between CPI and BT is depicted in Fig. S1B. There was a significant increase from 0.35 to 0.70 mM, but it remained almost constant after a further increase. However, there was a substantial rise in the substitution degree with increased BT concentration. The rise in the BT ratio in the critical ratio may cause the improvement in the substitution degree observed [43]. These analyses confirmed the strong binding affinity of BT for CPI and the successful synthesis of the CPI-BT conjugate. The CPI-BT 1.05 mM with the optimum grafting was selected for most of the following characterizations (represented as CPI-BT in the subsequent parts of the work).

3.2. Characterization of CPI-BT conjugate

3.2.1. Structural characterization of CPI-BT

FTIR was used to characterize the protein's secondary structural changes after grafting. As shown in Fig. 2A, four distinct peaks attributed to amide A (~3372.74 cm^{-1}), amide I (~1652.21 cm^{-1}), amide II (~1545.61 cm^{-1}), and amide III (~1396.98 cm^{-1}) were observed. These bands were altered in the conjugates as opposed to the native protein in terms of peak position and shape, suggesting modifications to the secondary structure of CPI. The intensities of the amide peaks increased and became more evident as the BT concentration increased. Compared to the control CPI, the intensity of the amide II peak in CPI-BTs spectra was noticeably higher. This elevation in intensity could be due to the increased number of amide linkages resulting from the binding of phenolic compounds to the proteins [39]. These bonds, C-O, C-N, and C-S are responsible for the peak at 1224.22 cm^{-1} that emerged after the conjugation process [44]. The CPI-BT's protein conformation was also examined using CD spectroscopy. From Fig. 2B, there was an apparent difference between the CPI and CPI-BT spectra trends. There was a remarkable decrease in the molar ellipticity and a blue shift of the peak from 197.02 nm (CPI) to 192.84 nm (CPI-BT). There was also a significant negative attenuation of the peak found at 225 nm, indicating the loss of α-helix structure in CPI.

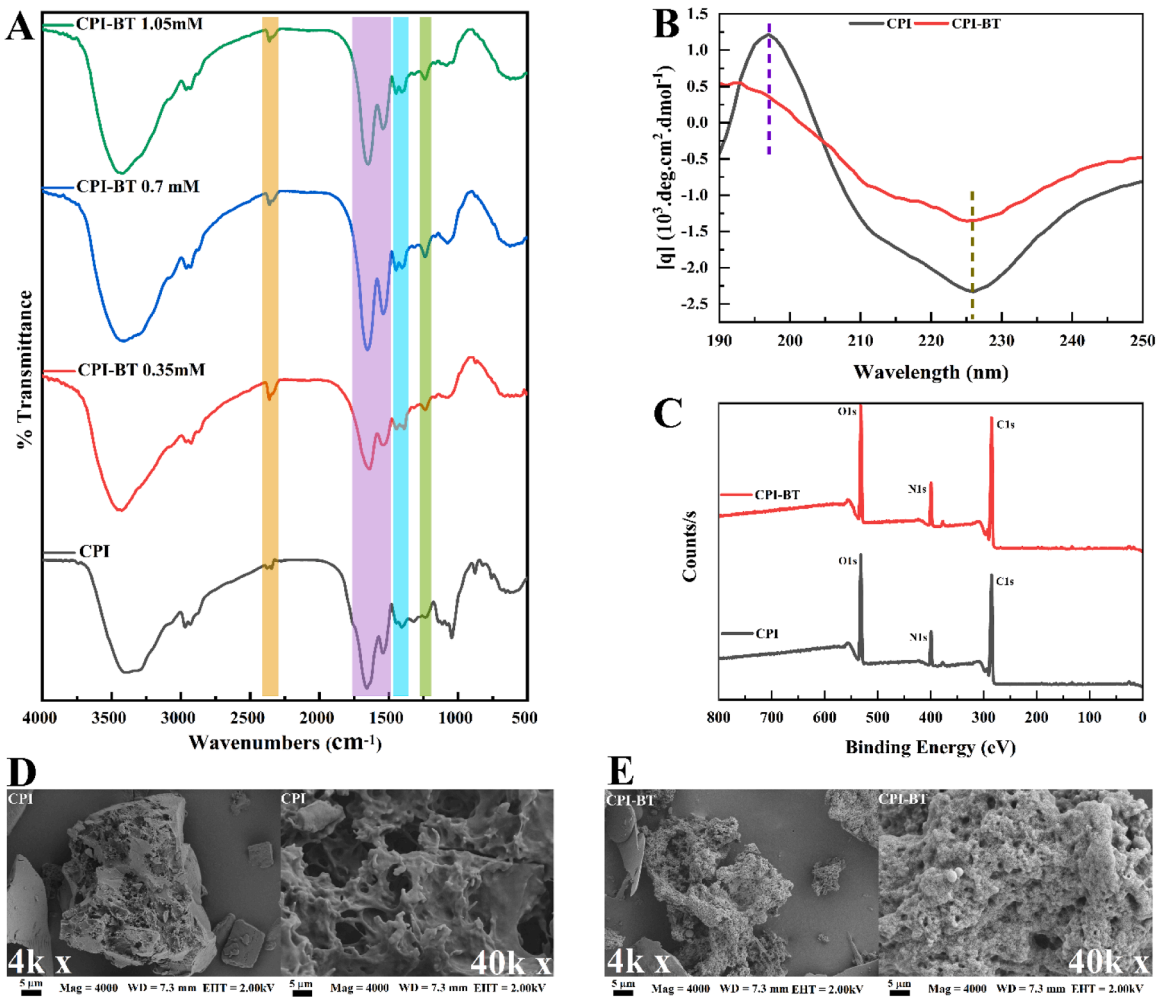

Fig. 2. FTIR spectra of CPI, CPI-BT 0.35, CPI-BT 0.7, and CPI-BT 1.05 mM (A), Far-UV CD spectra of CPI and CPI-BT (B), XPS spectra of CPI and CPI-BT (C); SEM images of CPI (D) and CPI-BT (E).

This loss suggested that molecular unfolding occurred within the protein structure [23]. The conjugation resulted in changes in the ellipticity, which indicated that the overall gross structure was not maintained, and the process altered CPI's conformation and converted the structural content among the protein secondary structures.

CPI's surface was primarily composed of C, N, and O, as shown in Fig. 2C. Following the conjugation, the XPS pattern of CPI-BT showed no discernible new band emergence and was comparable to the native CPI. Nonetheless, the characteristic peak at 400 eV, associated with the aromatic C═N and C-N, showed a noticeably higher intensity. Three major chemical components to the spectra were identified using high resolution of the C1s, notably C–C/C–H, C═O, and C–O/C–N, as seen in Fig. S2A. The spectra were further deconvoluted to explain the change in O status in the samples; the broad O1s peak yielded two O components, as shown in Fig. S2B. The first is mainly attributed to O═C at a binding energy of around 531.1 eV, and the second to O–H/C at a binding energy of about 532.4 eV. The O1s features have comparable shapes and binding energies, indicating that the oxygen-containing species in all samples are similar. Three N1s peaks were observed in the spectra of the CPI and CPI-BT, as shown in Fig. S2C. The amide N assigned at 399.8 ± 0.2 eV was observed to drastically increase from CPI to CPI-BT, while the other two peaks decreased. The SEM images revealed that the particles of CPI samples were compact with a relatively smooth and tight structure, as shown in Fig. 2D. However, the CPI-BT particles were relatively loose, with an increase in roughness and tiny pores on their surface.

3.2.2. *Physicochemical properties of CPI-BT*

The effect of the conjugation reaction on the carboxyl content of CPI is depicted in Fig. 3A. Increasing the concentration from 0.35 to 1.05 mM resulted in an increase in the carboxyl group present in the sample. The carboxyl content for CPI was 1.13×10^{-3} , which increased to 1.31×10^{-3} for CPI-BT 1.05 mM. The increase ratio was relatively lower than previously studied deamidated CPI (CPH) samples [34]. Since BT's structure doesn't include carboxyl groups, their presence wouldn't increase the conjugate's overall count. However, protein deamidation may result from low levels of ascorbic acid and H_2O_2 (the redox system used for conjugation in this study) [33]. The amide groups, especially asparagine, can be attacked by the free radicals generated during the conjugation, resulting in mild deamidation and conversion to aspartic acid [45]. Because the reaction conditions are not harsh, that could be the reason why the increase in the carboxyl content was not high. This is confirmed by the FTIR spectra (Fig. 2A), the peak around ~1540 cm^{-1} , representing the increased carboxylic groups. This contributed to the improvement of the amphiphilic ratio of CPI.

Fig. 3A depicts the zeta potential of CPI and CPI-BT. There was a substantial increase in the absolute value of CPI-BT's zeta-potential compared to CPI. The phenolic hydroxyl groups in polyphenols can become charged or ionized based on the pH environment [46]. This can, therefore, change a protein's overall surface charge density when a charged polyphenol forms a covalent bond with it, adding more charges to the surface. Also, the increase in carboxyl groups on the protein molecular chain can lead to an increase in the negative charge of the

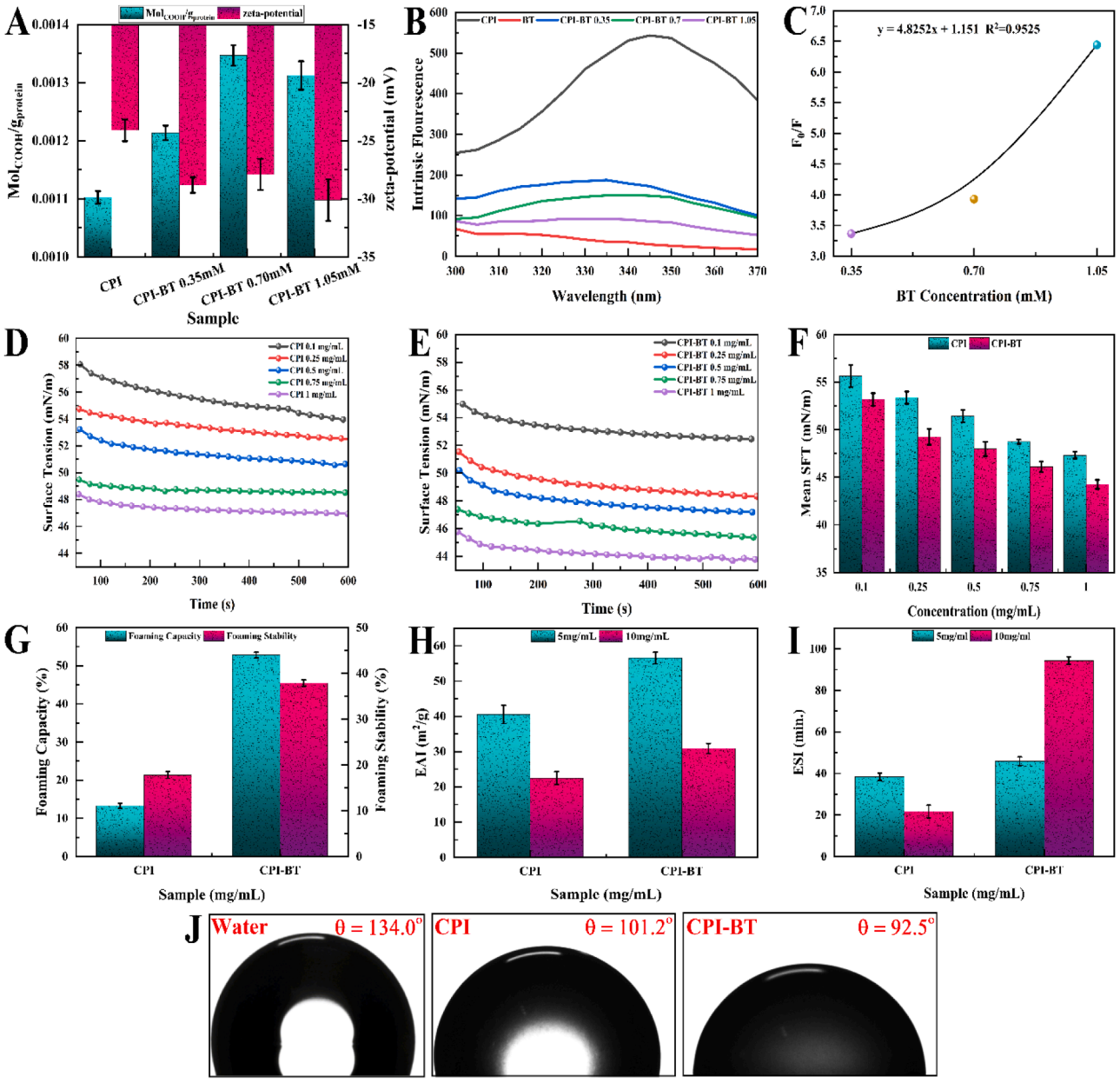

Fig. 3. Carboxyl content ($Mol_{COOH}/g_{peptide}$) and zeta-potential (A), fluorescence intensity spectra (B), Stern-Volmer plots for the fluorescence quenching of CPI by BT (C), surface tension (SFT) of CPI (D) and CPI-BT solutions (E), mean SFT of CPI and CPI-BT (F), and foaming capacity and stability of CPI and CPI-BT (G), emulsifying activity index (H), emulsifying stability index (I), and contact angle of water, CPI, and CPI-BT solutions (J). Values with different superscripted letters are significantly different at $p < 0.05$.

molecular surface, which increases zeta potential [34]. So, at pH 7, CPI showed a substantial increase in the zeta potential with an increase in the BT concentration because more carboxyl groups were deprotonated at neutral pH. Fig. 3J shows the values and images of the contact angle of CPI and CPI-BT solutions on paraffin surfaces. The contact angle of 134.0° between water and the paraffin block surface indicates that the paraffin was almost not wetted. The contact angle decreased from 134.0° for water to 101.2° for CPI and reduced further to 92.5° for CPI-BT. This suggests that CPI-BT showed an improved hydrophilic character; this could be due to the presence of BT that was added to the CPI, which is highly hydrophilic.

The modification in the tertiary structure of CPI after the grafting was characterized using fluorescence spectroscopy. As shown in Fig. 3B, CPI had the highest emission maximum (λ_{max}) value compared with the CPI-BTs. With increasing BT concentration, the fluorescence intensity of the conjugates weakened. Intrinsic fluorescence, which depends on the environmental polarity of two aromatic amino acids, Trp and Tyr residues or Trp/Tyr specific interactions, is typically used as an indicator of changes in the tertiary structure of proteins [31]. These variations in fluorescence intensity demonstrated that Trp and Tyr were involved in the covalent interaction of CPI with BT. According to previous studies, covalent conjugation can cause enveloped Trp and Tyr in proteins to become exposed and react with polyphenols, lowering the fluorescence intensity [35,36]. This suggested the weakening of the hydrophobicity of CPI since the amino acids involved in the reaction are hydrophobic. It also indicates that BT quenched CPI due to the CPI-BT interaction. There are two types of fluorescent quenching: static and dynamic [37]. The fluorescence data was fitted using the Stern-Volmer equation to explain the fluorescence quenching process between CPI and BT. The linear Stern-Volmer graphs are categorized as static or dynamic quenching. As

opposed to this, the curved Stern-Volmer plots (concave toward the y-axis) are thought to represent a hybrid of static and dynamic quenching. From Fig. 3C, BT had both dynamic and static quenching mechanisms. The modified Stern-Volmer equation (Eq. 5) was used to calculate the K_q and K_{FQ} values (Table S1). The K_q values were significantly higher than the highest values of scatter collision quenching (2.0×10^{10} M^{-1} s^{-1}), suggesting a static quenching in most cases but a dynamic quenching in some cases [30].

Figs. 3D and 3E depict the surface tension changes over time at the water-air interface of CPI and CPI-BT solutions at different concentrations. Within the first 50 s, the surface tension declined rapidly before attaining a slow and steady rate of decline. With the extension of time, they reached equilibrium and leveled off. Protein molecules in an aqueous solution typically fold into a coil-like shape to conceal the hydrophobic regions in the coil's center and expose the hydrophilic groups to water. On the other hand, the protein will partially unfold and align its hydrophobic groups toward the air phase when it approaches the air-water interface [47]. Fig. 3F shows that CPI-B reduced the surface tension between the water and air phases more than CPI at all concentrations. CPI-BT had a better ability to reduce the surface tension, which could be due to the partial unfolding and improved amphiphilicity that occurred during the conjugation process.

3.2.3. Functional properties

Proteins' structural and functional characteristics are both impacted by conjugating proteins with polyphenols [46]. CPI's secondary and tertiary structural changes impact its surface charge density and spatial conformation, ultimately affecting its functionality [21,34]. From Fig. 3G, the FC and FS increased after the grafting reaction. Both samples had their foams decrease after standing for 30 min. The large interface between the gas and liquid phases, combined with the strong thermodynamic instability, can cause the seeping, weakening of the fluid film layer, gas diffusion, and defoaming of the bubble [48]. The FC of CPI-BT (52.8 %) was significantly higher than CPI (13.3 %). Consequently, the stability was increased considerably by the conjugation. An improvement in whey [49] and soy [36] proteins' ability to form foams after the covalent conjugation with polyphenols was demonstrated in previous studies.

The conjugate's EAI and ESI were higher than the CPI, as displayed in Figs. 3H and 3I. The concentration of proteins also greatly influenced the

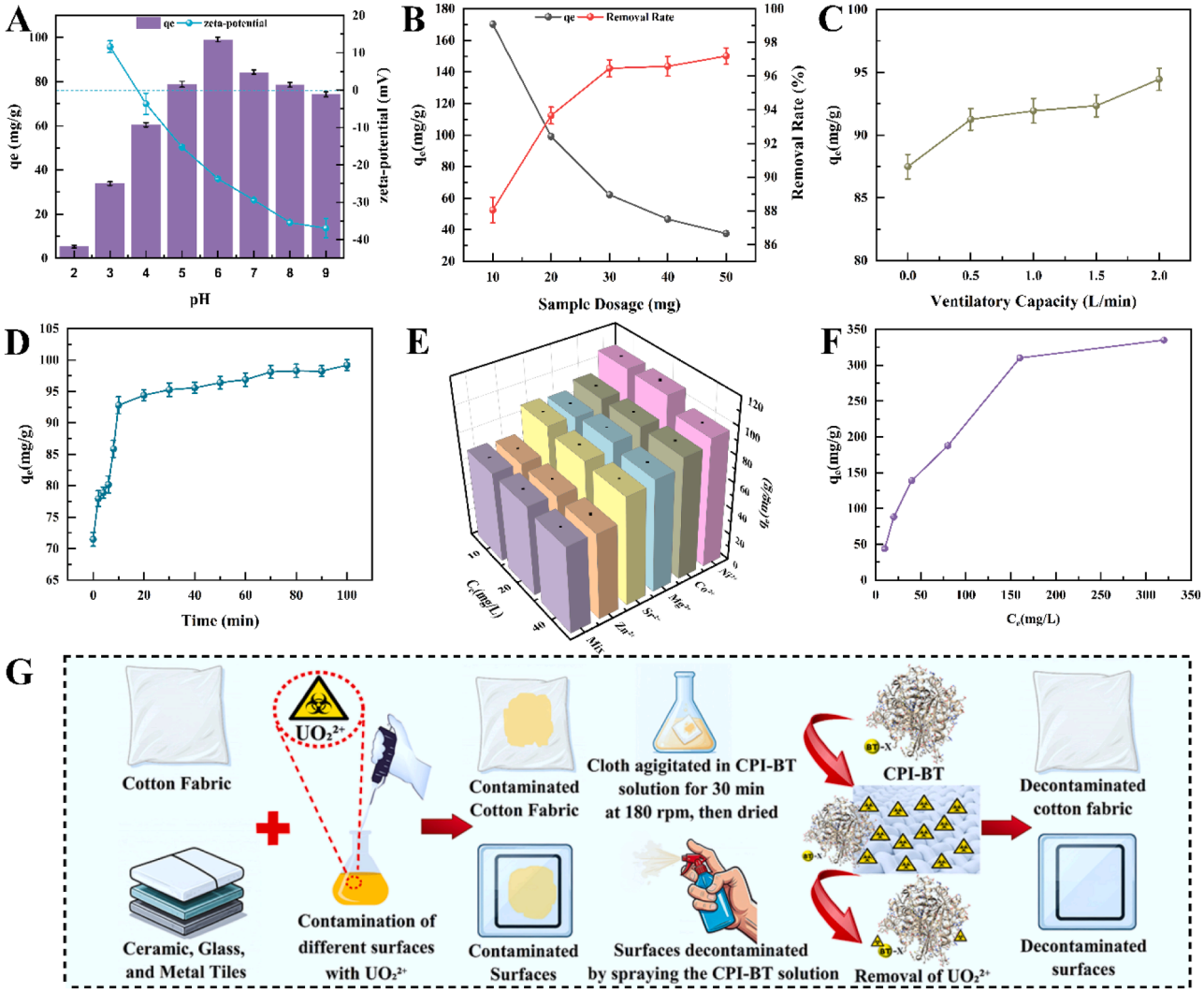

Fig. 4. Effect of pH on UO_2^{2+} removal (C_o = 20 mg/L, sample dosage = 20 mg, V = 0.1 L, T = 298.15 K, t = 30 min, VC = 2.0 L/min) and zeta-potential (A), effect of dosage sample on UO_2^{2+} removal (C_o = 20 mg/L, V = 0.1 L, T = 298.15 K, t = 30 min, pH = 6.0, VC = 2.0 L/min) (B), effect of ventilatory capacity on UO_2^{2+} removal (C_o = 20 mg/L, sample dosage = 20 mg, V = 0.1 L, T = 298.15 K, t = 30 min, pH = 6.0) (C), effect of contact time on UO_2^{2+} (C_o = 20 mg/L, V = 0.1 L, T = 298.15 K, sample dosage = 20 mg, pH = 6.0, VC = 2.0 L/min) (D), effect of coexisting ion systems on UO_2^{2+} removal (C_o = 20 mg/L, Ce = 10, 20, and 40 mg/L for the other cations, sample dosage = 20 mg, T = 298.15 K, V = 0.1 L, t = 30 min, pH = 6.0) (E), effect of initial concentration on UO_2^{2+} (V = 0.1 L, T = 298.15 K, sample dosage = 20 mg, t = 30 min, pH = 6.0, VC = 2.0 L/min) (F), and schematic decontamination by CPI-BT on the different surfaces (G).

EAI; declining values were observed as the concentration increased from 5 to 10 mg/mL for all samples. The data of CPI at 10 mg/mL, EAI (22.47 m^2/g), and ESI (21.7 min) was in a similar range to other reports of the emulsifying properties of different cultivars of CPI prepared at the same concentration, EAI and ESI values were 13.3–23.1 m^2/g and 17.3–29.6 min, respectively [21]. However, CPI-BT's EAI was 27.24 % higher than that of CPI. Also, the ESI values of the conjugate samples increased, which meant that the stability of the emulsions was much stronger compared with CPI. An improvement in rice bran protein hydrolysate [31], soy [36], and lactoferrin [35] proteins' ability to emulsify after covalent conjugation with polyphenols was demonstrated in prior investigations.

3.3. Ion flotation uranium removal performance

3.3.1. The effect of pH and sample dosage

The uranium adsorption by CPI-BT was initially investigated across a range of pH (2−9) values. This approach was adopted due to the significant influence of pH on both the speciation of uranium in solution and the surface charge characteristics of the adsorbent. The adsorption capacity of CPI-BT for UO_2^{2+} increased with increasing pH, reaching a maximum at pH 6 (Fig. 4A). Further increases in pH led to a decline in adsorption capacity in the alkaline region. The results demonstrated an upward and downward tendency of adsorption performances. The observed decrease in uranium adsorption at lower pH values can be attributed to the competition effect of protonation of the surfactant's functional groups, such as carboxylic acid and amino groups. At higher pH values, reduced adsorption is likely due to deprotonation of the functional groups, reducing the available binding sites, the strong competitive effect from carbonate complexation, and uranium hydrolysis [50]. An aqueous solution's initial pH influences uranium ions' speciation and charge, directly affecting their interaction with and binding affinity to adsorption materials [51]. Furthermore, the foam quickly forms at higher pH values, potentially hindering effective contact between the surfactant and the UO_2^{2+} ions. This rapid foam generation limits the accessibility of the surfactant to the target contaminant, resulting in a decrease in uranium removal efficiency. As a result, pH 6 was selected for all the subsequent tests. The surfactant's surface carries predominantly negative charges when pH > 3.0 (Fig. 4A). This negative surface charge facilitates electrostatic attraction between UO_2^{2+} ions and the surfactant [3]. Notably, as the pH increased, the absolute zeta-potential value increased, which correlated with a significant increase in the adsorption capacity of CPI-BT for UO_2^{2+} ions. These results further support understanding the pH-dependent adsorption behavior observed. As presented in Fig. 4B, the removal capacity for UO_2^{2+} steadily declined as the amount of CPI-BT increased from 10 to 50 mg; however, the removal rate of UO_2^{2+} dramatically increased. With the adsorbent dosage at 50 mg, the removal ratio of CPI-BT was 97.2 %, which indicated a high removal efficiency. This could be attributed to the increased surface area and availability of more binding sites in CPI-BT. In contrast, surplus reactive locations remained unsaturated due to the limited supply of UO_2^{2+} in solution. Given the relatively high adsorption capacity and removal ratio of CPI-BT, 20 mg was chosen as the optimal adsorbent dosage.

Fig. 4 C illustrates how ventilatory capacity, which ranged from 0 to 2.0 L/min, affects UO_2^{2+} removal performance. The foam developed more slowly at lower flow rates with a lower chance of entirely removing the ions. The increased ventilation capacity caused the UO_2^{2+} removal capacity to increase as the gas flow rate did, but this improvement was minimal. The reason could be that higher ventilatory capacity increased the bubble rupture and caused the ions stuck to the foam to separate.

3.3.2. The effect of equilibrium time

The amount of UO_2^{2+} removed by CPI-BT over time is displayed in Fig. 4D. The UO_2^{2+} was removed rapidly as time elapsed, peaking in less than 30 min. As a result, the adsorption equilibrium time was selected to be 30 min. Due to the adequate quantity of active chelating sites on CPI-BT, the removal process proceeded quickly. CPI-BT's sufficient binding sites can be rapidly chelated with UO_2^{2+} during the initial removal stage. Because fewer binding sites were available as the adsorption process continued, this slowed the removal rate. Two kinetic models, pseudo-first-order and pseudo-second-order, were employed to fit the acquired kinetic data to understand the adsorption mechanism. The fitting curve outcomes are displayed in Fig. S3 and Table S2. It can be observed that over 90 % of the equilibrium adsorption for UO_2^{2+} occurred during the initial 10 min and then ascended slowly during the next 90 min. The pseudo-second-order linear model provides a more accurate description of the elimination process. The pseudo-secondary model's calculation of the adsorption capacity of UO_2^{2+} ($q_{e\text{-}cal}$, 97.734 mg/g) was in close agreement with the actual result ($q_{e\text{-}exp}$, 99.077 mg/g). This outcome demonstrated that chemical reactions dominated the removal process.

3.3.3. The effect of coexisting ions

One of the challenging issues in the practical application of decontaminants is the selective separation of UO_2^{2+} because other metal ions are usually present in areas of radioactive contamination [25]. The selectivity of CPI-BT in adsorbing UO_2^{2+} from nuclear effluent comprising Co^{2+}, Mg^{2+}, Ni^{2+}, Sr^{2+}, and Zn^{2+} in binary and multi-ions solutions were examined (Fig. 4E). The experimental results show that CPI-BT has a high selectivity for UO_2^{2+}. The adsorption capacity remained high in the presence of these competing ions (Co^{2+}, Mg^{2+}, Ni^{2+}, and Sr^{2+}). The adsorption capacity did not change much with increasing or decreasing the initial concentration of these competing ions. This showed that other metal ions had no significant effect on UO_2^{2+} removal. However, the UO_2^{2+} adsorption capacity of CPI-BT declined by about 30 % in the presence of Zn^{2+} at all concentrations. This shows that CPI-BT possesses binding abilities for Zn^{2+}, which can be attributed to the protein components of the adsorbent [52]. A similar trend was observed in the multi-ions system, which can be mainly attributed to the presence of Zn^{2+}. Nonetheless, it appears that UO_2^{2+} dominates the adsorption sites of CPI-BT.

3.3.4. The effect of initial concentration and isotherm model

The impact of the initial UO_2^{2+} concentration on the CPI-BT removal properties was also examined, as Fig. 4F illustrates. The results indicated that the removal amount of UO_2^{2+} increased as the UO_2^{2+} concentration increased, reaching a maximum value of 310.15 mg/g. Because CPI-BT's binding sites were not completely occupied at lower concentrations of UO_2^{2+}, the amount of UO_2^{2+} removal increased quickly. In contrast, the binding sites on CPI-BT became occupied and unable to bind more UO_2^{2+} at high concentrations of UO_2^{2+}. Understanding the fundamental physicochemical behavior of the adsorption process, as shown by the adsorption isotherms, is crucial when researching this process. Thus, the Freundlich and Langmuir isotherm models described the adsorption processes of CPI-BT to UO_2^{2+} [53]. These models explain some parameters related to the removal mechanism, including the adsorbent's surface characteristics, affinity for the adsorbate, and removal capability [54]. The fitting results are displayed in Figs. S4A, S4B, and Table S3. CPI-BT's removal of UO_2^{2+} is observed to be well-suited to the Langmuir isothermal model with a regression coefficient of ($R^2 > 0.96$). This suggests that the adsorption took place on a homogeneous monolayer surface. The maximal elimination capacity of CPI-BT for UO_2^{2+}, as per the Langmuir model, was 224.72 mg/g. Table S4 compares CPI-BT with other comparable adsorbents that have been recently reported, and it shows that CPI-BT had better performance. The results show that the CPI-BT adsorption capacity calculated by the Langmuir model is greater than that of these adsorbents.

3.3.5. Desorption

The low adsorption capacity of CPI-BT at acidic pH levels (Fig. 4A) was leveraged to facilitate the efficient desorption of UO_2^{2+}. A pH 1.5

nitric acid solution was employed as the desorption reagent, achieving a desorption efficiency of up to 97 %. These results indicate that the UO_2^{2+} adsorbed onto CPI-BT can be effectively and easily recovered, highlighting the potential of this system for practical uranium recovery and recycling applications.

3.4. Characterization

To further understand the mechanism and confirm the removal of the UO_2^{2+} during the ion flotation test, other characterization analyses were performed in that regard. Fig. 5A shows the morphology and elemental composition of CPI-BT after the adsorption of UO_2^{2+}. After adsorbing UO_2^{2+}, the surface of CPI-BT had more pores, increased roughness, and a more granular shape. CPI-BT is mainly composed of C, O, and N atoms; however, a new peak appeared in the CPI-BT – U (Fig. 5A), which revealed that the UO_2^{2+} was adsorbed onto the conjugate. The corresponding elemental mapping images highlight that UO_2^{2+} is highly dispersed throughout the material, indicating that a significant portion of UO_2^{2+} had adsorbed on the CPI-BT's active sites. It also confirms that the UO_2^{2+} was absorbed onto the surface of CPI-BT, as was suggested by the Langmuir model in the previous section. Several peak intensities were enhanced or diminished, and a new peak appeared after the adsorption of UO_2^{2+} as displayed in the FTIR spectrum (Fig. 5B). A new peak appeared at 914 cm^{-1} , which can be attributed to the stretching vibrations of the O═U═O [55]. This proved that the UO_2^{2+} was successfully chelated with CPI-BT. The peak at 3430 cm^{-1} , attributed to the strong stretching vibrations of –OH and –NH [49], became wider. Also, the peak at 1224 cm^{-1} , a typical peak of the phenolic hydroxyl group [8], significantly became weaker; this demonstrated that the removal of UO_2^{2+} included the phenolic hydroxyl group.

The XPS spectra of CPI-BT before and after the ion flotation analysis are depicted in Fig. 5C. The ion flotation of UO_2^{2+} resulted in the appearance of a new signal peak in the XPS full spectrum, which is designated as U4f and suggests the successful adsorption of UO_2^{2+} onto CPI-BT. This was consistent with the FTIR and EDS analyses. The high-resolution spectrum of U4f after uranium adsorption revealed the presence of both U(VI) and U(IV) species. Peaks at 380.40 eV and 391.25 eV (U 4 $f_{5/2}$) were characteristic of U(IV), while peaks at 382.09 eV and 392.90 eV correspond to U(VI), indicating the reduction of U(VI) to U(IV) on the surfactant [50]. CPI contains electron-rich amino acids such as cysteine, tyrosine, and tryptophan, and BT contains phenolic hydroxyl groups that can promote reduction [2,20]. These functional groups can act as electron donors, transferring electrons to U(VI) and reducing them to U(IV) [56]. Also, the amphiphilic nature of CPI-BT can create microenvironments that favor electron transfer reactions. The observed reduction suggests that CPI-BT may absorb uranium and contribute to its immobilization and potential detoxification. In the N1s XPS high-resolution spectrum, three peaks

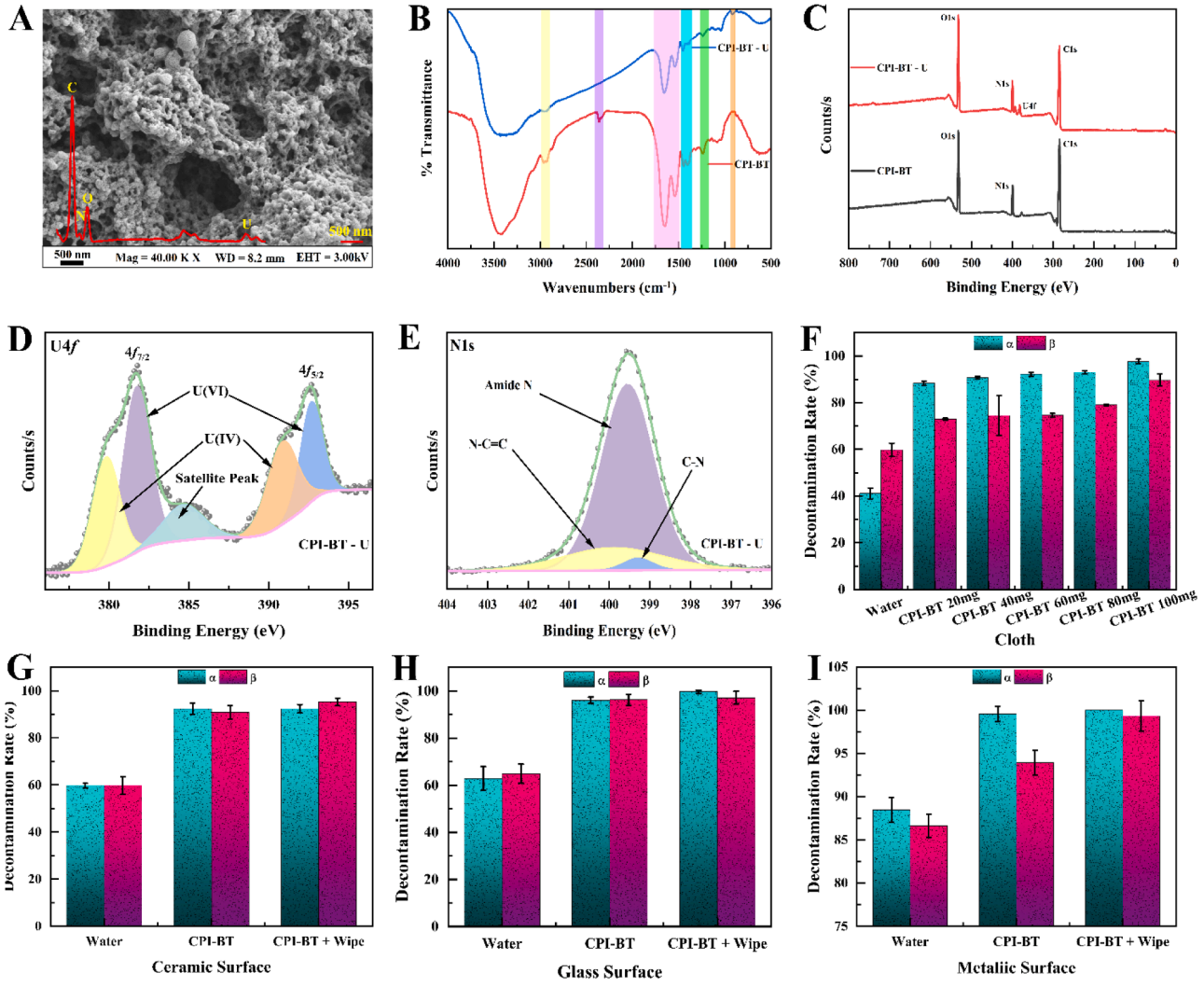

Fig. 5. SEM and EDS image of CPI-BT–U (A), FTIR spectra of CPI-BT and CPI-BT–U (B), XPS spectra of CPI-BT and CPI-BT–U (C), U4f of CPI-BT–U (D), N1s of CPI-BT–U (E), efficiency of CPI-BT decontamination on different surfaces including cotton fabric (F), ceramic tile (G), glass (H), and metal (I).

similar to the native CPI-BT were observed. However, the peaks at 400.68 eV, 399.38 eV, and 397.98 eV in CPI-BT shifted. After treatment with UO_2^{2+}, the peak generally assigned to C-N shifted to 399.28 eV. This shift could be due to changes in the electron density around the N atoms upon interaction with uranium. The electron density of N decreased due to the attraction of the outer electrons caused by the positive metal ions, which led to a higher bonding energy [57]. In the O1s XPS high-resolution spectrum, the two overlapping peaks in Fig. S6 at 532.28 eV and 530.98 eV correspond to C═O and C-O-R, respectively [34]. The peak corresponding to C-O-R had a shift in its original peak from 531.08 eV following the UO_2^{2+} adsorption. This could be because the O atom's external electrons were drawn to positive metal ions, increasing their bonding energy [25]. It also indicated that the carboxyl groups on CPI were engaged in the adsorption process. By covalent bonding, the –NH and the –C═O groups can contribute a lone electron pair and chelate with UO_2^{2+} [58]. CPI-BT adsorption for UO_2^{2+} is due mainly to the chelating process between UO_2^{2+} and the phenolic hydroxyls of BT and CPI's active sites.

3.5. Decontamination by CPI-BT on different surfaces

To increase the range of applications for CPI-BT, additional research was done on the removal effect of UO_2^{2+} on solid surfaces. The contaminated cotton fabric material was washed with water or CPI-BT solution, and the amount of UO_2^{2+} removed after the washing process was determined. The decontamination rate (DR) of CPI-BT is shown in Fig. 5F. The results show that CPI-BT demonstrated a good removal efficiency, with a removal rate of 88.4 %. The DR for UO_2^{2+} significantly increased as the amount of CPI-BT increased from 20 to 100 mg. Comparable morphology free of surface degradation was also visible in the cotton fabric's SEM images, as shown in Figs. S7A-C. The distribution diagram indicated that the uranium element was uniformly dispersed on the surface of the cotton fabric, and the CPI-BT removed it within 30 minutes. The DR value calculated from the EDS data for the CPI-BT decontaminated cloth was in a similar range as the DR value for CPI-BT 20 mg. The CPI-BT solution was also used to decontaminate simulated radionuclides on ceramic tile, glass, and metal surfaces. The decontamination involves spraying and wetting the surface with CPI-BT solution, which causes the radionuclide to dissolve and diffuse within the solution. Due to the adequate quantity of active chelating sites on CPI-BT, the complexation, adsorption, and redox reactions with the active functional groups aided the decontamination process. The results of the DR are shown in Fig. 5G-I. For all the surfaces, the DR values were significantly high and greater than 90 %. There was a 35.30 %, 34.55 %, and 11.16 % increase in the DR for ceramic tile, glass, and metal surfaces compared to just water. Also, the surfaces washed with just water had faint traces of yellow coloration after washing for the ceramic and glass tile, as shown in Fig. S8. CPI-BT can effectively remove UO_2^{2+} from different surfaces in less time than water. Applying wipes soaked in the CPI-BT solution resulted in higher DR values > 95 % for all surfaces; however, this increase was marginal compared with the CPI-BT solution. Since radioactive contaminants are primarily physically bonded to these materials' surfaces [6], the contaminants dissolve readily in the CPI-BT solution, which readily eliminates the simulated radionuclides.

3.6. Possible mechanism

The possible schematic model of the adsorption mechanism of UO_2^{2+} onto CPI-BT is shown in Fig. 6. The experimental analysis and theoretical calculations suggest that chelation is the main mechanism of UO_2^{2+} adsorption onto CPI-BT. The ortho-phenolic hydroxyl groups on BT's ring can be ionized into negative oxygen, and the carboxylic acid groups in amino acids such as aspartic and glutamic acids can form carboxylate ions, which act as strong ligands and chelate the UO_2^{2+}. The UO_2^{2+} adsorption also relies on the ability of CPI-BT's functional groups to transfer electrons. During UO_2^{2+} adsorption, electrons may be transferred directly to U(VI), facilitating its reduction and complexation. The electron-rich amino acid residues of CPI can contribute electron lone pairs to the empty electronic orbitals of UO_2^{2+}, forming stable chelates.

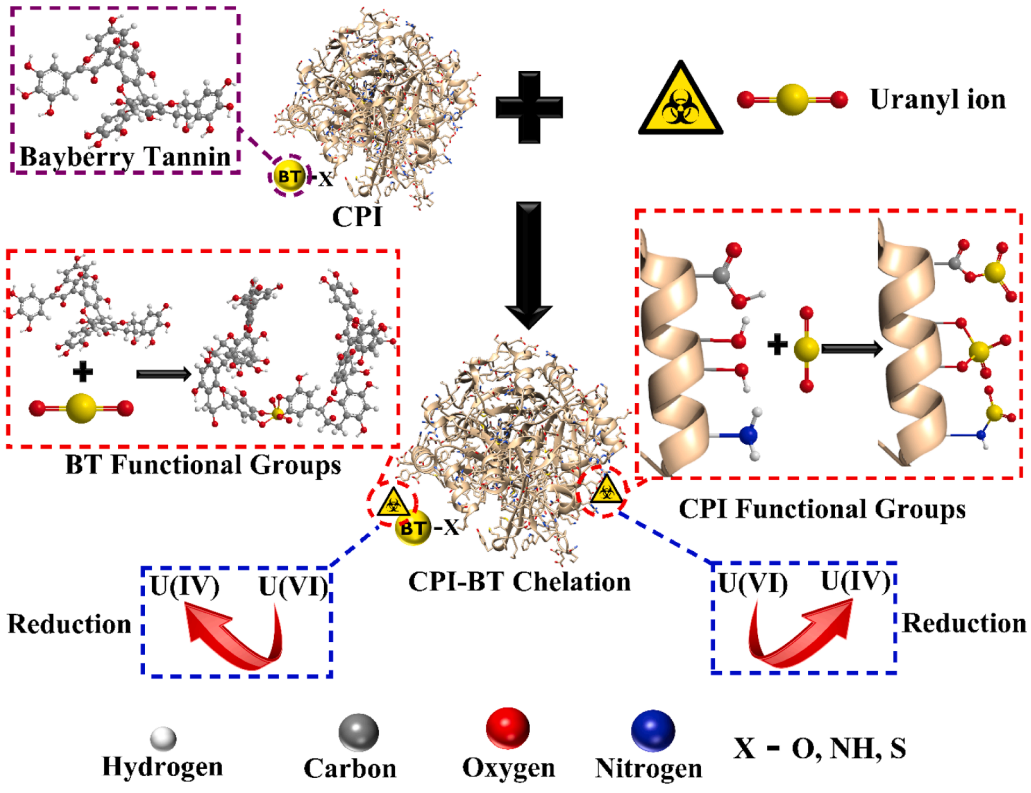

Fig. 6. Schematic process of UO_2^{2+} adsorption mechanism onto CPI-BT.

4. Conclusion

This study synthesized a green surfactant using the ascorbic acid/H_2O_2 redox pair initiator system to covalently conjugate CPI with BT to form a CPI-BT. Free radical grafting is an eco-friendly and green chemistry procedure. The results confirmed the effective grafting of the polyphenol onto the protein. The quenching mechanism of CPI by BT was by both dynamic and static quenching. The conjugation process altered CPI's structural and physicochemical properties and induced conformational changes in the protein molecules. The interaction weakened the hydrophobicity and increased the hydrophilicity, leading to improved amphiphilicity. The conjugation was effective in improving the protein's foaming and emulsifying properties. Particularly, CPI-BT can efficiently remove UO_2^{2+} in water environments and different solid surfaces. At an initial concentration of 320 mg/L of UO_2^{2+}, ion flotation achieved a maximum removal capacity of 310.15 mg/g. CPI-BT also exhibited good adsorption selectivity in several coexisting ion systems. The UO_2^{2+} adsorption onto CPI-BT can be mainly attributed to the phenolic hydroxyl groups of BT and the amino and carboxyl groups of CPI. These groups chelate with UO_2^{2+}, forming stable chelates; thus, CPI-BT conjugate is a promising alternative to chemical surfactants. The observed reduction during the chelation suggests that CPI-BT can absorb uranium and contribute to its immobilization and potential detoxification. The present findings provide new insights into applying CPI-BT as a safe and low-cost surfactant in the remediation of radionuclide-polluted water environments or solid surfaces near uranium mining operations and nuclear facilities.

Environmental implication

The global use of synthetic surfactants has significant environmental impacts, however managerial and policy measures to mitigate these effects remain predominantly insufficient. A green, protein-based surfactant derived from agro-industrial waste offers a sustainable solution for the remediation of uranium removal. By leveraging bayberry tannin's binding properties and cottonseed protein's structural versatility, this novel surfactant provides a safer and more eco-friendly alternative to chemical decontaminants. It adheres to green-chemistry principles, minimizing hazardous chemicals' use and waste generation. The surfactant's biodegradability further contributes to its environmental sustainability. By effectively removing uranium from both aqueous and solid surfaces, this technology can help mitigate the risks associated with uranium contamination.

CRediT authorship contribution statement

Xue Min: Supervision, Resources, Funding acquisition. **Kuang Meng:** Supervision, Resources. **Wei Yanxia:** Writing – review & editing, Supervision, Funding acquisition. **Frempong Akosua Nyame Adom:** Writing – review & editing. **Liang Xiaofang:** Formal analysis. **Chen Yu:** Data curation. **Liu Xiaobo:** Validation. **Frempong Kwame Eduam Baiden:** Writing – original draft, Visualization, Methodology, Investigation, Formal analysis, Data curation, Conceptualization. **Wang Jie:** Resources, Funding acquisition, Formal analysis. **Zhou Jian:** Writing – review & editing, Supervision, Resources, Project administration, Conceptualization.

Declaration of Competing Interest

The authors declare that they have no known competing financial interests or personal relationships that could have appeared to influence the work reported in this paper.

Acknowledgments

The authors thank the financial support from the Xinjiang Science and Technology Major Project (2024A02001), Xinjiang Key Research and Development Program (2022B02039-3), and State Key Laboratory of Cotton Bio-breeding and Integrated Utilization Open Fund (CB2024A03).

Conflict of interest

All authors declare that they do not have any conflict of interest.

Appendix A. Supporting information

Supplementary data associated with this article can be found in the online version at doi:10.1016/j.jhazmat.2025.137450.

Data Availability

Data will be made available on request.

References

[1] Yan, R.-H., Cui, W.-R., Zhang, C.-R., Li, X.-J., Huang, J., Jiang, W., et al., 2021. Bio-inspired hydroxylation imidazole linked covalent organic polymers for uranium extraction from aqueous phases (Article). Chem Eng J 420, 129658. https://doi.org/10.1016/j.cej.2021.129658.
[2] Yu, J., Luo, X., Liu, B., Zhou, J., Feng, J., Zhu, W., et al., 2018. Bayberry tannin immobilized bovine serum albumin nanospheres: characterization, irradiation stability and selective removal of uranyl ions from radioactive wastewater. J Mater Chem A 6 (31), 15359–15370. https://doi.org/10.1039/c8ta05000g.
[3] Li, Y., Li, X.-X., Wang, Z.-Y., Zhang, F., Wu, Q., Sha, L.-T., et al., 2022. Design and synthesis of a novel bifunctional polymer with malonamide and carboxyl group for highly selective separation of uranium (VI). Sep Purif Technol 302, 122115. https://doi.org/10.1016/j.seppur.2022.122115.
[4] Kaminski, M.D., Lee, S.D., Magnuson, M., 2016. Wide-area decontamination in an urban environment after radiological dispersion: a review and perspectives. J Hazard Mater 305, 67–86. https://doi.org/10.1016/j.jhazmat.2015.11.014.
[5] Grives, S., Phan, G., Morat, G., Suhard, D., Rebiere, F., Fattal, E., 2015. Ex vivo uranium decontamination efficiency on wounded skin and in vitro skin toxicity of a calixarene-loaded nanoemulsion. J Pharma Sci 104 (6), 2008–2017. https://doi.org/10.1002/jps.24431.
[6] Yoon, I.-H., Kim, S.E., Choi, M., Kim, S., Choi, W.-K., Jung, C.-H., 2020. Highly enhanced foams for stability and decontamination efficiency with a fluorosurfactant, silica nanoparticles, and Ce(IV) in radiological application. Environ Technol Innov 18, 100744. https://doi.org/10.1016/j.eti.2020.100744.
[7] Zhu, Y., Fan, W., Zhou, T., Li, X., 2019. Removal of chelated heavy metals from aqueous solution: a review of current methods and mechanisms. Sci Total Environ 678, 253–266. https://doi.org/10.1016/j.scitotenv.2019.04.416.
[8] Zhang, A., Li, X., Xing, J., Xu, G., 2020. Adsorption of potentially toxic elements in water by modified biochar: a review. J Environ Chem Eng 8 (4), 104196. https://doi.org/10.1016/j.jece.2020.104196.
[9] Singh, S., Kapoor, D., Khasnabis, S., Singh, J., Ramamurthy, P.C., 2021. Mechanism and kinetics of adsorption and removal of heavy metals from wastewater using nanomaterials. Environ Chem Lett 19 (3), 2351–2381. https://doi.org/10.1007/s10311-021-01196-w.
[10] Chang, L., Cao, Y., Fan, G., Li, C., Peng, W., 2019. A review of the applications of ion floatation: wastewater treatment, mineral beneficiation and hydrometallurgy. RSC Adv 9 (35), 20226–20239. https://doi.org/10.1039/C9RA02905B.
[11] Hu, N., Liu, W., Jin, L., Li, Y., Li, Z., Liu, G., et al., 2017. Recovery of trace Cu^{2+} using a process of nano-adsorption coupled with flotation: SNP as an adsorbing carrier. Sep Purif Technol 184, 257–263. https://doi.org/10.1016/j.seppur.2017.05.009.
[12] Peng, W., Chang, L., Li, P., Han, G., Huang, Y., Cao, Y., 2019. An overview on the surfactants used in ion flotation. J Mol Liq 286, 110955. https://doi.org/10.1016/j.molliq.2019.110955.
[13] Cserháti, T., Forgács, E., Oros, G., 2002. Biological activity and environmental impact of anionic surfactants. Environ Int 28 (5), 337–348. https://doi.org/10.1016/S0160-4120(02)00032-6.
[14] Bouyer, E., Mekhloufi, G., Rosilio, V., Grossiord, J.L., Agnely, F., 2012. Proteins, polysaccharides, and their complexes used as stabilizers for emulsions: alternatives to synthetic surfactants in the pharmaceutical field? Int J Pharm 436 (1-2), 359–378. https://doi.org/10.1016/j.ijpharm.2012.06.052.
[15] Johnson, P., Trybala, A., Starov, V., Pinfield, V.J., 2021. Effect of synthetic surfactants on the environment and the potential for substitution by biosurfactants. Adv Colloid Interface Sci 288, 102340. https://doi.org/10.1016/j.cis.2020.102340.
[16] Pradhan, A., Bhattacharyya, A., 2017. Quest for an eco-friendly alternative surfactant: Surface and foam characteristics of natural surfactants. J Clean Prod 150, 127–134. https://doi.org/10.1016/j.jclepro.2017.03.013.
[17] Sharma, J., Sundar, D., Srivastava, P., 2023. Advantages and Disadvantages of Biosurfactants over Other Synthetic Surfactants. In: Aslam, R., Mobin, M., Aslam, J., Zehra, S. (Eds.), Advancements in Biosurfactants Research. Springer

International Publishing, Cham, pp. 505–523. https://doi.org/10.1007/978-3-031-21682-4_23.
[18] Kumar, M., Hasan, M., Choyal, P., Tomar, M., Gupta, O.P., Sasi, M., et al., 2022. Cottonseed feedstock as a source of plant-based protein and bioactive peptides: evidence based on biofunctionalities and industrial applications. Food Hydrocoll 131, 107776. https://doi.org/10.1016/j.foodhyd.2022.107776.
[19] Kumar, M., Tomar, M., Punia, S., Grasso, S., Arrutia, F., Choudhary, J., et al., 2021. Cottonseed: a sustainable contributor to global protein requirements. Trends Food Sci Technol 111, 100–113. https://doi.org/10.1016/j.tifs.2021.02.058.
[20] Wang, L., Ma, M., Yu, Z., Du, S.K., 2021. Preparation and identification of antioxidant peptides from cottonseed proteins. Food Chem 352, 129399. https://doi.org/10.1016/j.foodchem.2021.129399.
[21] Ma, M., Ren, Y., Xie, W., Zhou, D., Tang, S., Kuang, M., et al., 2018. Physicochemical and functional properties of protein isolate obtained from cottonseed meal. Food Chem 240, 856–862. https://doi.org/10.1016/j.foodchem.2017.08.030.
[22] Frempong, K.E.B., He, G., Kuang, M., Xue, M., Wang, J., Wei, Y., et al., 2024. Sulfonated cottonseed hydrolysates with adjustable amphiphilicity as environmental -Stress stable emulsifiers. Food Chem 454, 139787. https://doi.org/10.1016/j.foodchem.2024.139787.
[23] Chen, K., Chen, X., Liang, L., Xu, X., 2020. Gallic acid-aided cross-linking of myofibrillar protein fabricated soluble aggregates for enhanced thermal stability and a tunable colloidal state. J Agric Food Chem 68 (41), 11535–11544. https://doi.org/10.1021/acs.jafc.0c02059.
[24] Li, M., Mu, Y., Xu, Q., Jin, L., Fu, Y., 2024. Injectable, rapid self-healing, antioxidant and antibacterial nanocellulose-tannin hydrogels formed via metal-ligand coordination for drug delivery and wound dressing. Ind Crops Prod 208, 117876. https://doi.org/10.1016/j.indcrop.2023.117876.
[25] Chen, J., Frempong, K.E.B., Ding, P., He, G., Zhou, Y., Kuang, M., et al., 2023. Plant polyphenol surfactant construction with strong surface activity and chelation properties as efficient decontamination of UO_2^{2+} on cotton fabric. Int J Biol Macromol 254 (Pt 2), 127451. https://doi.org/10.1016/j.ijbiomac.2023.127451.
[26] Sun, X., Huang, X., Liao, X.-p, Shi, B.J.Johm, 2010. Adsorptive recovery of UO_2^{2+} from aqueous solutions using collagen–tannin resin. J Hazard Mater 179 (1-3), 295–302. https://doi.org/10.1016/j.jhazmat.2010.03.002.
[27] Sun, X., Huang, X., Liao, X.-p, Shi, B.J.Johm, 2011. Adsorptive removal of Cu (II) from aqueous solutions using collagen-tannin resin. J lHazardous Mater 186 (2-3), 1058–1063. https://doi.org/10.1016/j.jhazmat.2010.11.098.
[28] Zou, Y., Wan, Z., Guo, J., Wang, J., Yin, S., Yang, X., 2017. Tunable assembly of hydrophobic protein nanoparticle at fluid interfaces with tannic acid. Food Hydrocoll 63, 364–371. https://doi.org/10.1016/j.foodhyd.2016.09.010.
[29] Jing, Y., Diao, Y., Yu, X., 2019. Free radical-mediated conjugation of chitosan with tannic acid: characterization and antioxidant capacity. React Funct Polym 135, 16–22. https://doi.org/10.1016/j.reactfunctpolym.2018.12.005.
[30] Gong, T., Tian, D., Hu, C.Y., Guo, Y.R., Meng, Y.H., 2022. Improving antioxidant ability of functional emulsifiers by conjugating polyphenols to sodium caseinate. Lwt 154, 112668. https://doi.org/10.1016/j.lwt.2021.112668.
[31] Wang, S., Li, X., Zhu, J., Liu, H., Liu, T., Yu, G., et al., 2021. Covalent interaction between high hydrostatic pressure-pretreated rice bran protein hydrolysates and ferulic acid: focus on antioxidant activities and emulsifying properties. J Agric Food Chem 69 (27), 7777–7785. https://doi.org/10.1021/acs.jafc.1c01949.
[32] Feng, Y., Jin, C., Lv, S., Zhang, H., Ren, F., Wang, J., 2023. Molecular mechanisms and applications of polyphenol-protein complexes with antioxidant properties: a review. Antioxid (Basel) 12 (8), 1577. https://doi.org/10.3390/antiox12081577.
[33] Chen, L., Xie, X., Li, Y., Xiong, H., Li, L., 2022. Activation mechanism of whey protein isolate mediated by free radicals generated in the ascorbic acid/hydrogen peroxide system (Article). Food Chem 384, 132533. https://doi.org/10.1016/j.foodchem.2022.132533.
[34] Frempong, K.E.B., He, G., Kuang, M., Jun, P., Xue, M., Wei, Y., et al., 2023. Improvement of amphipathic properties with molecular structure unfolding and activation of cottonseed protein as ultra stable and safe emulsifier by deamidation. Int J Biol Macromol, 125802. https://doi.org/10.1016/j.ijbiomac.2023.125802.
[35] Liu, F., Sun, C., Yang, W., Yuan, F., Gao, Y., 2015. Structural characterization and functional evaluation of lactoferrin–polyphenol conjugates formed by free-radical graft copolymerization. RSC Adv 5 (20), 15641–15651. https://doi.org/10.1039/c4ra10802g.
[36] Sui, X., Sun, H., Qi, B., Zhang, M., Li, Y., Jiang, L., 2018. Functional and conformational changes to soy proteins accompanying anthocyanins: focus on covalent and non-covalent interactions. Food Chem 245, 871–878. https://doi.org/10.1016/j.foodchem.2017.11.090.
[37] Ferrer-Gallego, R., Goncalves, R., Rivas-Gonzalo, J.C., Escribano-Bailon, M.T., de Freitas, V., 2012. Interaction of phenolic compounds with bovine serum albumin (BSA) and alpha-amylase and their relationship to astringency perception. Food Chem 135 (2), 651–658. https://doi.org/10.1016/j.foodchem.2012.04.123.
[38] Joshi, M., Adhikari, B., Aldred, P., Panozzo, J.F., Kasapis, S., Barrow, C.J., 2012. Interfacial and emulsifying properties of lentil protein isolate. Food Chem 134 (3), 1343–1353. https://doi.org/10.1016/j.foodchem.2012.03.029.
[39] Mohammadi, A., Kashi, P.A., Kashiri, M., Bagheri, A., Chen, J., Ettelaie, R., et al., 2023. Self-assembly of plant polyphenols-grafted soy proteins to manufacture a highly stable antioxidative Pickering emulsion gel for direct-ink-write 3D printing. Food Hydrocoll 142, 108851. https://doi.org/10.1016/j.foodhyd.2023.108851.
[40] Zhang, K., Huang, J., Wang, D., Wan, X., Wang, Y., 2024. Covalent polyphenols-proteins interactions in food processing: formation mechanisms, quantification methods, bioactive effects, and applications. Front Nutr 11, 1371401. https://doi.org/10.3389/fnut.2024.1371401.
[41] Spizzirri, U.G., Iemma, F., Puoci, F., Cirillo, G., Curcio, M., Parisi, O.I., et al., 2009. Synthesis of antioxidant polymers by grafting of gallic acid and catechin on gelatin. Biomacromolecules 10 (7), 1923–1930. https://doi.org/10.1021/bm900325t.
[42] Curcio, M., Puoci, F., Iemma, F., Parisi, O.I., Cirillo, G., Spizzirri, U.G., et al., 2009. Covalent insertion of antioxidant molecules on chitosan by a free radical grafting procedure. J Agric Food Chem 57 (13), 5933–5938. https://doi.org/10.1021/jf900778u.
[43] Ozdal, T., Capanoglu, E., Altay, F., 2013. A review on protein–phenolic interactions and associated changes. Food Res Int 51 (2), 954–970. https://doi.org/10.1016/j.foodres.2013.02.009.
[44] Sun, D., Ban, R., Zhang, P.-H., Wu, G.-H., Zhang, J.-R., Zhu, J.-J., 2013. Hair fiber as a precursor for synthesizing of sulfur- and nitrogen-co-doped carbon dots with tunable luminescence properties. Carbon 64, 424–434. https://doi.org/10.1016/j.carbon.2013.07.095.
[45] Robinson, N.E., 2002. Protein deamidation. Natl Acad Sci USA 99, 5283–5288 https://doi.org/https://www.pnas.org/doi/abs/10.1073/pnas.082102799.
[46] Li, M., Ritzoulis, C., Du, Q., Liu, Y., Ding, Y., Liu, W., et al., 2021. Recent progress on protein-polyphenol complexes: effect on stability and nutrients delivery of oil-in-water emulsion system. Front Nutr 8, 765589. https://doi.org/10.3389/fnut.2021.765589.
[47] Pugnaloni, L.A., Dickinson, E., Ettelaie, R., Mackie, A.R., Wilde, P.J., 2004. Competitive adsorption of proteins and low-molecular-weight surfactants: computer simulation and microscopic imaging. Adv Colloid Interface Sci 107 (1), 27–49. https://doi.org/10.1016/j.cis.2003.08.003.
[48] Yu, M.A., Damodaran, S., 1991. Kinetics of protein foam destabilization: evaluation of a method using bovine serum albumin. J Agric Food Chem 39 (9), 1555–1562. https://doi.org/10.1021/jf00009a004.
[49] Jia, Z., Zheng, M., Tao, F., Chen, W., Huang, G., Jiang, J., 2015. Effect of covalent modification by (–)-epigallocatechin-3-gallate on physicochemical and functional properties of whey protein isolate. LWT - Food Sci Technol 66. https://doi.org/10.1016/j.lwt.2015.10.054.
[50] Zhang, Y., Wang, Y., Dong, Z., Wang, Y., Liu, Y., Cao, X., et al., 2024. Boosting uranium extraction from Seawater by micro-redox reactors anchored in a seaweed-like adsorbent. Nat Commun 15 (1), 9124. https://doi.org/10.1038/s41467-024-53366-3.
[51] Pu, Y., Qiang, T., Li, G., Ruan, X., Ren, L., 2023. Efficient adsorption of low-concentration uranium from aqueous solutions by biomass composite aerogel. Ecotoxicol Environ Saf 259, 115053. https://doi.org/10.1016/j.ecoenv.2023.115053.
[52] Yu, J., Liao, H., Zhu, W., Duan, T., Wang, S., Kuang, M., et al., 2019. Marinobacter sp. Stable hydrous titanium oxide-functionalized bovine serum albumin nanospheres for uranium capture from spiked seawater. ACS Appl Mater Interfaces 11 (43), 40898–40908. https://doi.org/10.1021/acsami.9b14542.
[53] Mahmoud, D.K., Salleh, M.A.M., Karim, W.A.W.A., Idris, A., Abidin, Z.Z., 2012. Batch adsorption of basic dye using acid treated kenaf fibre char: equilibrium, kinetic and thermodynamic studies. Chem Eng J 181-182, 449–457. https://doi.org/10.1016/j.cej.2011.11.116.
[54] Billah, R.E.K., Kaya, S., Şimşek, S., Halim, E.M., Agunaou, M., Soufiane, A., 2023. Removal and regeneration of As(V) in aqueous solutions by adsorption on calcined fluorapatite. Int J Environ Sci Technol 20 (5), 5197–5206. https://doi.org/10.1007/s13762-022-04459-3.
[55] Gao, P., Hu, Y., Shen, Z., Zhao, G., Cai, R., Chu, F., et al., 2024. Ultra-highly efficient enrichment of uranium from seawater via studtite nanodots growth-elution cycle. Nat Commun 15 (1), 6700. https://doi.org/10.1038/s41467-024-50951-4.
[56] Lv, Z., Yang, S., Chen, L., Alsaedi, A., Hayat, T., Chen, C., 2019. Nanoscale zero-valent iron/magnetite carbon composites for highly efficient immobilization of U (VI). J Environ Sci 76, 377–387. https://doi.org/10.1016/j.jes.2018.06.001.
[57] Kong, W., Li, Q., Liu, J., Li, X., Zhao, L., Su, Y., et al., 2016. Adsorption behavior and mechanism of heavy metal ions by chicken feather protein-based semi-interpenetrating polymer networks super absorbent resin. RSC Adv 6 (86), 83234–83243. https://doi.org/10.1039/C6RA18180E.
[58] Senanayake, S.D., Waterhouse, G.I.N., Chan, A.S.Y., Madey, T.E., Mullins, D.R., Idriss, H., 2007. The reactions of water vapour on the surfaces of stoichiometric and reduced uranium dioxide: a high resolution XPS study. Catal Today 120 (2), 151–157. https://doi.org/10.1016/j.cattod.2006.07.040.